

Theoretical investigation of the Ag filament morphology in conductive bridge random access memories

Kan-Hao Xue, Yun Li, Hai-Lei Su, Jun-Hui Yuan, Yi Li, Zhuo-Rui Wang, Biao Zhang, and Xiang-Shui Miao^{a)}

Wuhan National Research Center for Optoelectronics, School of Optical and Electronic Information, Huazhong University of Science and Technology, Wuhan 430074, China

(Received 30 May 2018; accepted 30 August 2018; published online 8 October 2018)

Conductive bridge random access memories (CBRAMs) usually involve active Ag or Cu metals, where the formation of metal filaments accounts for the low resistance state. For the application of neuromorphic computation, it is highly desirable to develop artificial neurons and synapses, which utilize the complicated volatile or nonvolatile resistive switching phenomena, respectively. This can be achieved by controlling the morphology and stability of the filaments, which requires a deep understanding of the filament formation and disruption mechanisms. Using *ab initio* calculations, we explored the physical mechanism behind various Ag filament morphologies and growth modes, using GeSe, ZrO₂, SiO₂, and a-Si as the examples. The roles of Ag and Ag⁺ stability inside the dielectric, the migration barrier of Ag⁺, and the Ag⁺ solvation effect have been investigated in detail. A comprehensive model has been proposed, which in particular could explain the diverse Ag filament morphology experimentally observed in sputtered SiO₂ and PECVD SiO₂. Our theoretical approach can serve as a pre-screening method in designing new solid-state electrolyte materials of CBRAM, aiming at new functionalities in neuromorphic computation or in-memory logic computing. *Published by AIP Publishing.* <https://doi.org/10.1063/1.5042165>

I. INTRODUCTION

Reproducible memory switching behavior enables the nonvolatile tuning of resistance state upon the electric voltage pulse input and is a key device characteristic for artificial synapse in neuromorphic computation.¹ The volatile threshold switching phenomenon provides the possibility to integrate input stimuli and fire action potential spikes, mimicking the critical features of neuron, i.e., the second building block for neuromorphic systems.² Memristors^{3,4} are undoubtedly one of the most promising candidate devices for such purposes,⁵ but the nonvolatile and volatile resistive switching mechanisms can be quite complex within the scope of memristors. Traditionally, two fundamental working principles dominate the resistive switching devices, namely, valence change mechanism (VCM) and electrochemical metallization mechanism (ECM).⁶ For VCM, the most ordinary device consists of a metal oxide dielectric layer sandwiched by two metal electrodes, where the local generation of a sufficient concentration of oxygen vacancies in the dielectric lowers the valency of the metal element, which finally yields electrical conduction paths. Nevertheless, the exact composition and structure of the resulting conductive filaments (CFs) are under intensive debate for many materials.^{7–11} On the contrary, it is usually believed that the working principles of ECM memories are more straightforward. Consider, for example, the Ag(Cu)/electrolyte/Pt system where Ag or Cu is the active electrode, Pt serves as the inert electrode, and the electrolyte may be liquids or solids such as certain oxides

and chalcogenides. Such a device is also named the conductive bridge random access memory (CBRAM), which relies on the formation and dissolution of the metal CFs. The ideal electroforming model for CBRAM is stated as follows. The active metal (such as Ag and Cu) is first oxidized into cations at the active anode, which migrate under the applied electric field toward the inert cathode (such as Pt). The cations are reduced at the cathode/electrolyte interface, generating neutral metal atoms there, the accumulation of which yields the CF. Hence, the growth direction of the CF should be from the inert electrode to the active electrode, which has been directly verified by the scanning electron microscope (SEM) observation by Guo *et al.*¹² where liquid water was used as the electrolyte.

Nevertheless, several recent transmission electron microscopy (TEM) experiments have shown that in many solid-state electrolyte materials [e.g., ZrO₂ and amorphous silicon (a-Si)] the CFs start to grow from the active electrode. In the literature, this phenomenon has been attributed to the low mobility of active metal ions.¹³ Furthermore, even if the CF growth direction is from the inert electrode to the active Ag electrode, the morphology of the Ag CFs could be either conical or dendritic, which has been attributed to the different electrochemical reaction rates at the cathode.¹⁴ Therefore, the cation mobility and the electrochemical reaction rates have been listed as two key parameters for the CF morphology. Nevertheless, it is more helpful if the morphology of the CFs can be predicted through first-principles calculations on the solid-state electrolyte material. In neuromorphic computation applications, it is highly desired that the morphology and stability of the CFs may be well controlled. For such special purposes, we envisage a bottom-up material design

^{a)}Email: miaoxs@hust.edu.cn

approach, where particular solid-state electrolyte materials may be predicted to yield the desired CF morphology. Or this approach can be used to screen out a number of candidate solid-state electrolytes in the materials genome engineering approach.¹⁵ Besides, the underlying physics related to the various CF morphologies in CBRAMs is still not completely understood yet, thus investigation into this issue with emphasis on the solid-state electrolyte material properties can provide valuable insights for the development of artificial neuron and synapse devices.

In this work, we shall use *ab initio* calculations to investigate the key factors that render the various Ag filament morphologies. Our theoretical approach involves the following aspects: (i) the capability of Ag^+ in keeping its charge in the dielectric; (ii) the mobility of Ag^+ in the dielectric; and (iii) the solvation effect of Ag^+ , if treating the dielectric as a solid-state electrolyte.

The paper is organized as follows. We shall first review the existing experimental evidences on the Ag CF morphology (including chalcogenides, ZrO_2 , SiO_2 , and a-Si). Then, we evaluate each dielectric material with emphasis on the three factors listed above. Finally, we extract the physical rules for the filament morphology, draw comprehensive conclusions, and make some predictions with respect to other solid-state electrolytes.

II. REVIEW OF EXPERIMENTAL EVIDENCES ON THE AG FILAMENT MORPHOLOGY

Early experimental observations confirm that the metal CF grows from the inert electrode side in liquid polar electrolytes and solid-state chalcogenides. Guo *et al.*¹² obtained clear images of dendrite-like Ag CFs that grow from the inert Pt electrode, when liquid water is used as the electrolyte. In chalcogenides which are regarded as solid-state electrolytes with supreme cation mobility, several experimental evidences also support that the CF starts to grow from the inert electrode, though Cu instead of Ag was used as the active electrode.^{16,17}

In 2012, Liu *et al.* observed the dynamic formation procedure of CFs in $\text{Ag}(\text{Cu})/\text{ZrO}_2/\text{Pt}$ CBRAM cells using TEM.¹⁸ It was surprisingly discovered that the Ag CFs started to grow from the active electrode, being thinner on the inert electrode side. During RESET, accordingly, the CFs broke near the inert electrode. Such an abnormal growth direction of the CFs was attributed to the low mobility of metal cations in the oxide electrolyte.^{18,19} During the migration process of the metal cations, they have high possibility to meet the electrons coming from the Pt cathode, i.e., the unavoidable leakage current. Hence, the reduction of Ag^+ into Ag occurs within the dielectric and possibly very close to the active anode. With the continuation of the oxidation/reduction processes, the accumulation of metal atoms at the anode/oxide interface leads to the nucleation. The nucleus then serves as an extension of the anode, which provides a fast track for metal ions migrating to the next nuclei due to the enhanced electric field. As this process continues, the tip of the CF gradually proceeds until it reaches the cathode. The same Ag CF morphology has been reported recently in $\text{Ag}/\text{TiO}_2/\text{Pt}$ and $\text{Ag}/\text{HfO}_x/\text{Pd}$ cells,^{20,21} where Ti and Hf

belong to the same group of elements as Zr. In both works, TEM images confirm that the diameter of the Ag CF is larger near the active Ag electrode, which serves as the anode during the SET process of memory switching.

Also in 2012, Yang *et al.* managed to observe unambiguously the dynamic formation of CFs in Ag/SiO_2 (or a-Si)/Pt CBRAM cells using TEM.²² The results show that the Ag CFs in SiO_2 started to grow from the inert electrode, but the morphology of the CF was a bit unexpected in that it was thinner near the inert electrode. Accordingly, the CF also broke on the inert electrode side during the RESET operation. However, in a-Si, the Ag CF proceeded from the active electrode during electroforming, and it was thinner near the inert electrode where the rupture of the CF normally occurs during RESET. They also conclude that mobility is a major factor in the growth dynamics of Ag CFs, whose significance may overwhelm the principle from traditional CBRAM model that the Ag CF should grow from the inert electrode.

In 2017, Yuan *et al.* confirmed the formation dynamics of Cu CFs within a $\text{Cu}/\text{SiO}_2/\text{W}$ CBRAM cell using *in situ* TEM.²³ It was discovered that Cu CFs also grow from the active electrode, and a typical CF exhibits an inverted cone shape with diameters of ~ 14 nm and ~ 10 nm near the Cu and W electrodes, respectively. The low mobility of Cu in SiO_2 was believed to be the key reason why the filament growth is kinetically limited by the cation supply instead of the reduction rate.

In sum, the complexity of the CF morphology and growth dynamics implies that the mobility of the cation itself is insufficient to explain all the experimental phenomena, though it is indeed a very important factor that needs to be explored in our research.

III. COMPUTATIONAL METHOD

Density functional theory (DFT) calculations were carried out using the plane-wave-based Vienna *Ab initio* Simulation Package (VASP).^{24,25} The generalized gradient approximation (GGA) was used for the exchange-correlation energy, within the Perdew–Burke–Ernzerhof (PBE) functional.²⁶ The electrons considered as in the valence were 4d and 5s for Ag; 4s, 4p, 4d, and 5s for Zr; 3s and 3p for Si; 2s and 2p for O; 4s and 4p for Ge; 4s and 4p for Se. Core electrons were approximated by projector augmented-wave pseudopotentials.^{27,28} The plane-wave kinetic energy cutoff was fixed to 500 eV, and sufficiently dense Monkhorst-Pack k -meshes²⁹ were utilized to sample the Brillouin zone. All bulk crystal structures were fully relaxed until the stress in each direction was less than 500 MPa, while all atomic coordinates were relaxed until the Hellmann-Feynman forces were below $0.02 \text{ eV } \text{\AA}^{-1}$.

The models for a-Si and amorphous- SiO_2 were generated using the standard melt-and-quench approach.³⁰ The crystalline Si (216 atoms) and SiO_2 (64 Si atoms and 128 O atoms) were used for the initial structures. They were melted at 2000 K for 2 ps and 2300 K for 1.2 ps, respectively, followed by cooling down for 1 ps. Finally, the structures were fully relaxed until the Hellmann-Feynman forces were below $0.02 \text{ eV } \text{\AA}^{-1}$ and the stress in each direction was less than 1

GPa. The densities of our a-Si and SiO₂ supercells are 2.36 g cm⁻³ and 2.17 g cm⁻³, respectively. The latter is very close to the experimental value 2.20 g cm⁻³,³¹ but for a-Si the typical experimental atomic density is 4.81×10^{22} cm⁻³,³² corresponding to a mass density of 2.24 g cm⁻³. Hence, we also set up a comparative a-Si supercell with vacancies to exactly match the experimental mass density. For GeSe and ZrO₂, we utilized their crystalline structures because they are easily crystallized under thermal budgets.

IV. RESULTS AND DISCUSSIONS

For each solid-state electrolyte, we carry out a series of studies including the spatial location of the Ag interstitial (Fig. 1), the charge states of nominal Ag and Ag⁺ inside the electrolyte (Table I), the solvation effect for Ag⁺ (Fig. 2), as well as the migration barrier of Ag and Ag⁺ (Table II and Fig. 3), where the typical CF morphology is shown in Fig. 4. We use undoped stoichiometric phases of the electrolytes, where the only defects are Ag and Ag⁺ interstitials.

A. GeSe

The case of GeSe is studied first of all because it is a typical chalcogenide material that serves as a standard cation conductor,³³ which ought to yield “standard” CBRAM behaviors. It is worthwhile to note that in Se-rich Ag-Ge-Se electrolytes there can be conductive Ag₂Se phase separated, as reported by Kozicki *et al.*^{33,34} In order to exclude the possibility of Ag₂Se CFs since we focus on metal Ag CFs, we built up a 72-atom stoichiometric GeSe supercell with 36 Ge atoms and 36 Se atoms, after which an additional Ag interstitial atom was introduced. The whole supercell after structural relaxation is demonstrated in Fig. 1(a). The Ag interstitial is located in a gap region far from surrounding atoms. It is closest to a Ge atom with an Ag-Ge bond length of 2.49 Å, and forming two more Ag-Ge bonds both with 2.90 Å bond

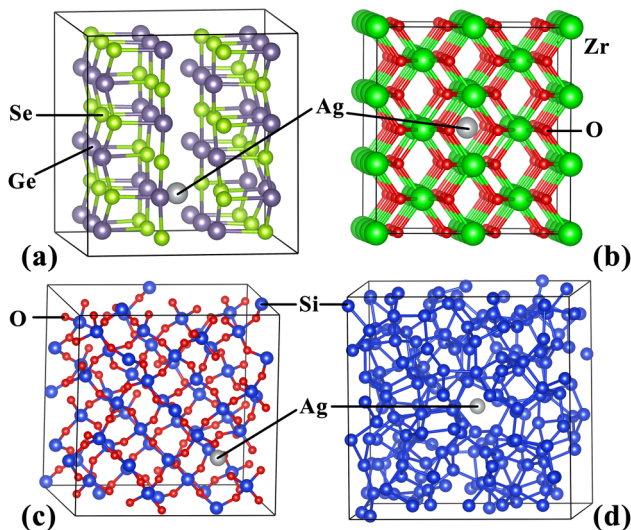


FIG. 1. Fully optimized supercell structures for (a) GeSe; (b) ZrO₂; (c) amorphous SiO₂; and (d) a-Si, each cell with one Ag interstitial atom introduced.

TABLE I. Apparent charge states of Ag/Ag⁺ within the dielectrics, according to Bader analysis.

Materials	Ag (<i>e</i>)	Ag ⁺ (<i>e</i>)
GeSe	+0.10	+0.12
ZrO ₂	+0.57	+0.58
SiO ₂	+0.16	+0.72
a-Si	+0.04 (+0.035)	+0.04 (+0.042)

length. Meanwhile, three Ag-Se bonds exist with bond lengths of 2.63 Å, 2.69 Å, and 2.69 Å, respectively.

Although we set up an electrically neutral supercell, there is no guarantee that the Ag interstitial should remain neutral as it can exchange electrons with the surrounding environment. Hence, we implemented the Bader analysis to investigate the charge state of the Ag interstitial inside GeSe. As listed in Table I, the Ag interstitial is indeed not neutral, but with +0.10 *e* charge according to Bader analysis. Subsequently, we subtracted one electron from the supercell, and after structural relaxation we calculated the Bader charge for the apparent Ag⁺ cation interstitial. Interestingly, its charge state according to Bader analysis is +0.12 *e*, very close to the Ag atom interstitial case. These results indicate that the charge state of silver inside GeSe is relatively fixed, and at least +0.10 *e* Bader charge guarantees that positively charged Ag ions can exist in the GeSe solid-state electrolyte. After removing the electron, the three Ag-Ge bond lengths become 2.48 Å, 2.87 Å, and 2.87 Å, while the three Ag-Se bond lengths become 2.63 Å, 2.70 Å, and 2.70 Å. The bond lengths are almost unchanged, revealing that the charge

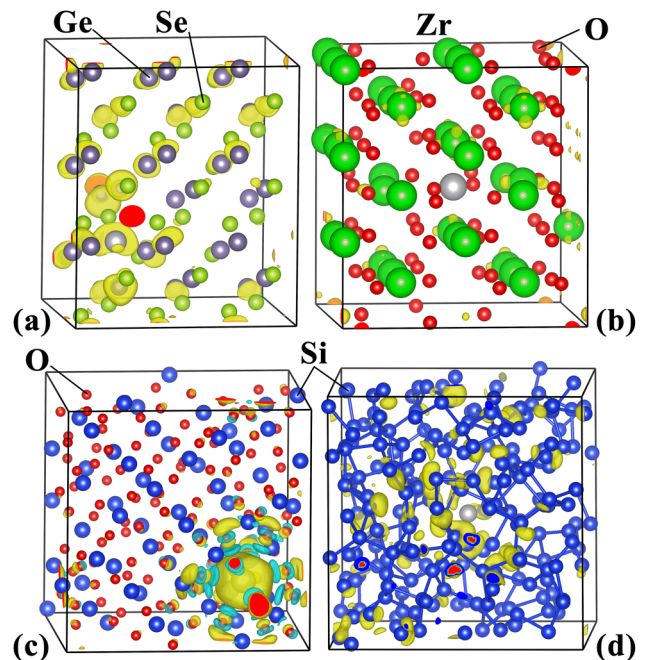


FIG. 2. Differential charges between supercells with an Ag-atom interstitial and that with an Ag⁺ interstitial: (a) GeSe; (b) ZrO₂; (c) SiO₂; and (d) a-Si. The charge contours are set to critical charge densities of $0.002 e \text{ \AA}^{-3}$, $0.01 e \text{ \AA}^{-3}$, $0.01 e \text{ \AA}^{-3}$, and $0.001 e \text{ \AA}^{-3}$, respectively.

TABLE II. Migration energy barriers for Ag/Ag⁺ within the four dielectrics under investigation.

Dielectrics	Migration barrier (eV)		Hopping distance (Å)
	Ag	Ag ⁺	
GeSe	0.19	0.20	3.8
ZrO ₂	2.39	2.48	3.6
SiO ₂	0.61	0.53	5.0
a-Si	0.99	0.98	4.6

status of the silver interstitial is relatively constant upon the electron removal.

It is a natural and relevant question how the charge distribution has been modified upon the removal of one whole electron from each supercell. To better visualize the charge distribution evolution, we calculated the differential charge density distribution by subtracting the electron density of the Ag⁺ case from that of the Ag atom case. Yet, in doing this, we did not relax the structure when the electron was removed. The benefit is clear that all the atoms are fixed to the same positions, which enables better visualization. As shown in Fig. 2(a), indeed only a small proportion of charge differences come from the Ag atom/ion. Rather, the surrounding Ge atoms mainly suffer the charge removal. Such results further confirm the relatively fixed (slightly ionic) nature of silver inside GeSe, thus Ag⁺ can hardly be “reduced” within GeSe. Hence, the charged Ag ions should first reach the inert cathode, or the virtue cathode made of Ag, where they are further reduced into metal Ag.

In addition, we calculated the energy barriers for the migration of Ag and Ag⁺ in GeSe, respectively, using the nudged elastic band (NEB) method. The choice of migration path is illustrated in Fig. 3(a). As listed in Table II, the migration barriers for both Ag and Ag⁺ in GeSe are no more than 0.2 eV, indicating fast transport. For Ag⁺ the calculated 0.20 eV migration barrier supports that Ag⁺ tends to migrate quickly to the inert electrode, rather than accumulating into clusters inside GeSe. In sum, the morphology of the Ag CF inside GeSe is a standard one, which grows from the inert electrode and is narrower near the Ag electrode. A schematic of this CF growth mode is illustrated in Fig. 4(a).

For Ag in GeSe, the most striking feature derived from our calculations is that the charge status of an Ag interstitial is fixed according to the need of the surrounding electrolyte, such that the foreign Ag⁺ can hardly be reduced by the leakage current. To strengthen this point, we did some more tests on modified GeSe electrolytes. First of all, we introduced a Ge vacancy, which is a common defect in GeSe,³⁵ from the model in Fig. 1(a). Then, we placed an Ag or Ag⁺ interstitial on the vacancy site. After relaxation, the Bader charge of the Ag (Ag⁺) interstitial has become +0.21 *e* (+0.22 *e*). It is natural that both Ag and Ag⁺ become more positively charged due to the presence of the Ge vacancy, which requires more electron removal from the interstitial. Yet, even with Ge vacancies, one finds that the charge status of the Ag interstitial is not sensitive to electron addition/removal,

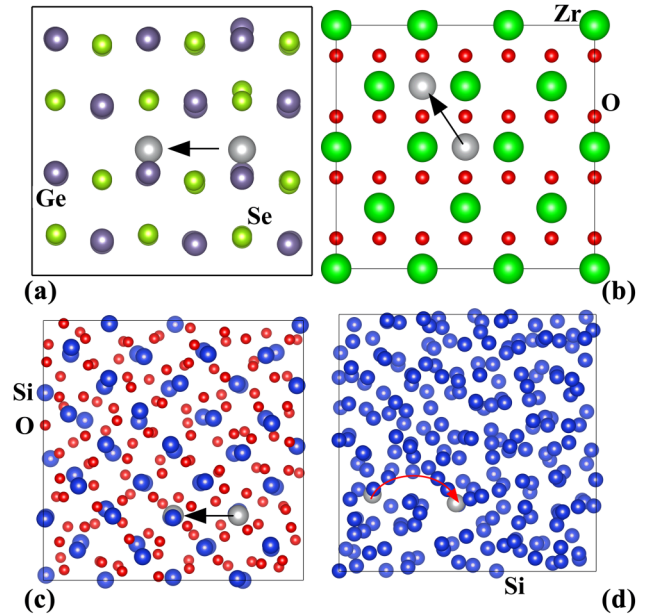


FIG. 3. Illustration of the approximate migration paths under investigation for Ag/Ag⁺ inside various dielectrics: (a) GeSe; (b) ZrO₂; (c) SiO₂; and (d) a-Si.

consistent with our previous finding in stoichiometric GeSe. Secondly, we examined the charge status of Ag in amorphous Ag₃₃Ge₂₀Se₄₇ by introducing either an Ag or an Ag⁺ interstitial in a supercell with 33 Ag, 20 Ge, and 47 Se atoms.³³ The Ag Bader charge ranges from +0.10 *e* to +0.34 *e* in the former case and from +0.10 *e* to +0.35 *e* in the latter case. In any case, most Ag atoms possess a Bader charge between +0.2 *e* and +0.3 *e*. Hence, even in Ag-abundant Ag-Ge-Se electrolytes, the charge status of a foreign Ag interstitial is not much influenced by electron addition/removal. This confirms that Ag⁺ tends to first reach the

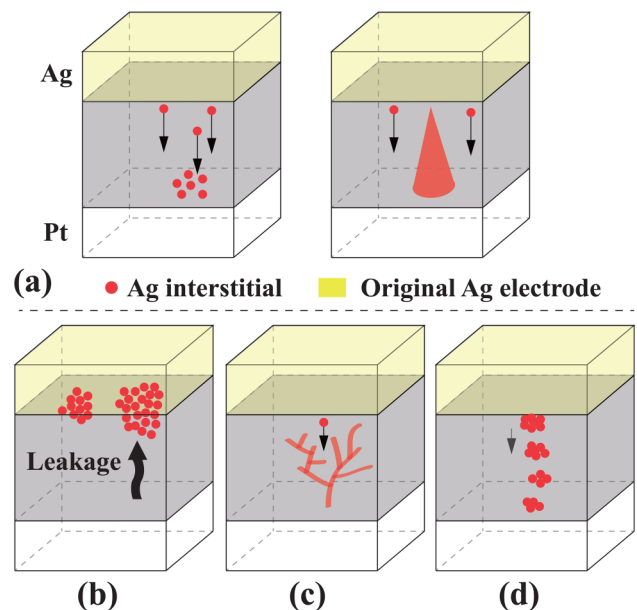


FIG. 4. Four typical models of Ag CF growth in various solid-state electrolytes: (a) GeSe; (b) ZrO₂; (c) sputtered SiO₂; (d) PECVD SiO₂ or a-Si.

counter inert electrode rather than being reduced inside the GeSe or Ag-Ge-Se electrolytes.

Having established the general rule for the “standard” CBRAM CF formation scheme [Fig. 4(a)], we now examine the case of Cu in GeTe where direct experimental evidence for such CF morphology was obtained.¹⁷ After introducing a copper interstitial in rhombohedral GeTe, we find that the Bader charges on the apparent Cu, Cu⁺, and Cu²⁺ interstitials are +0.07 *e*, +0.08 *e*, and +0.09 *e*, respectively. On the other hand, if there are pre-existing Ge vacancies, the foreign copper occupies a Ge vacancy site. In this case, the apparent Cu, Cu⁺ and Cu²⁺ interstitials exhibit Bader charges of +0.17 *e*, +0.18 *e*, and +0.18 *e*, respectively, demonstrating the same trend as Ag in GeSe. We infer that the observed standard CF morphology of Cu in GeTe is also due to the fact that the copper charge status is fixed by the chalcogenide electrolyte to a great extent.

B. ZrO₂

While GeSe belongs to a common class of solid-state electrolyte with fast cation transport, ZrO₂ belongs to another class of solid-state electrolyte which enables fast oxygen ion transport. Y-stabilized cubic ZrO₂ (YSZ) has been widely used as the electrolyte for solid oxide fuel cells.³⁶ It is interesting to compare ZrO₂ with GeSe in the field of CBRAM.

To this end, we calculated a 108-atom cubic ZrO₂ supercell with 36 Zr atoms and 72 O atoms. After introducing the silver interstitial, we calculated the differential charge between Ag and Ag⁺ in the material, as shown in Fig. 2(a). The Bader analysis indicates that the charge on Ag interstitial is +0.57 *e*, while for Ag⁺ interstitial the apparent charge is +0.58 *e*. Therefore, not only the existence of positively charged Ag cation is possible within ZrO₂, but it is even more difficult to obtain neutral Ag atoms inside ZrO₂. The reason is revealed by the differential charge, because one can see that the Ag interstitial strongly exchanges electrons with the surrounding Zr cations. Consequently, Zr is capable of varying its valency between +4 and +3, which is indeed common in chemistry. On the other hand, the influence of the Ag interstitial on the surrounding O anions is very minor.

Bond length analysis also indicates that there is almost no variation in the surrounding environment for the Ag interstitial, after it becomes an apparent Ag⁺ interstitial. In the former case, the neighboring Ag-O bond lengths for the interstitial are 2.32 Å, 2.32 Å, 2.34 Å, 2.34 Å, 2.40 Å, and 2.40 Å, while in the latter case they become 2.31 Å, 2.31 Å, 2.33 Å, 2.33 Å, 2.40 Å, and 2.40 Å, where the difference is negligible. For bond lengths to the surrounding Zr cations, in the former case we find 2.72 Å, 2.72 Å, 2.86 Å, 2.87 Å, 2.88 Å, and 2.90 Å, respectively. These values are almost identical to the latter case, i.e., 2.72 Å, 2.72 Å, 2.86 Å, 2.86 Å, 2.87 Å, and 2.89 Å.

Although silver is found to be positively charged inside ZrO₂, the following migration barrier calculation does not support that Ag⁺ can move fast inside ZrO₂. Indeed, the migration barriers are as large as 2.39 eV for Ag interstitial and 2.48 eV for Ag⁺ interstitial. The extremely low mobility implies that the Ag cations have high possibility to be

reduced by the leakage current, i.e., electron flow coming from the cathode. Hence, the growth mode of the Ag CF resembles the case of Fig. 4(b).

C. SiO₂

SiO₂ is an interesting solid-state electrolyte material for CBRAM, not only because it is very common and technically-compatible in microelectronics, but also due to the diversity of CF morphology when different deposition techniques are utilized. For sputtered SiO₂, the growth mode shown in Fig. 4(c) was discovered.²² With PECVD SiO₂, however, the mode shown in Fig. 4(b) usually dominates.³⁷

We calculated a 192-atom amorphous SiO₂ supercell, consisting of 64 Si atoms and 128 O atoms [Fig. 1(c)]. For the charge state of Ag and Ag⁺ interstitials, the Bader analysis reveals quite different results from GeSe and ZrO₂. The charge on Ag interstitial is +0.16 *e* while that on Ag⁺ interstitial is as large as +0.72 *e*. Therefore, there are two quite distinct states for the silver interstitial, and it is unambiguous whether or not the Ag⁺ has been reduced to Ag inside SiO₂. The differential charge analysis result shown in Fig. 2(c) confirms this point, because the Ag⁺ is shown to possess a clear solvation sphere surrounding it. Since the yellow and cyan colors represent positive and negative electron density changes, this clearly shows that the positively charged Ag⁺ possesses such a solvation shell with negative and positive bound charges located at the inner and outer surfaces, respectively.

The presence of the solvation shell also modifies the lengths of the bonds surrounding the interstitial. For the neutral Ag interstitial, its three shortest Ag-O bond lengths are 2.77 Å, 2.77 Å, and 2.77 Å, but these values are reduced significantly to 2.49 Å, 2.51 Å, and 2.59 Å when the interstitial becomes Ag⁺. This is caused by the strong Coulomb attraction between the Ag⁺ cation and the surrounding oxygen anions, which is the origin of the polarization effect as well.

Comparing ZrO₂ and SiO₂, we find that the charge status of silver inside the dielectric is almost fixed in the former, but is subject to variation in the latter. The reason is that ZrO₂ is mainly made of ionic bonds, but SiO₂ consists of covalent bonds. In addition, Zr can switch its valency between +3 and +4, thus it is primarily the valency of Zr that is adjusted upon the electron removal/addition, but the Ag interstitial always stays as a cation. In SiO₂, however, the saturation characteristic of Si-O covalent bonds forbids the strong variation of the Si valency. Hence, both Ag and Ag⁺ can be stable inside SiO₂.

On the kinetics aspect, the migration barriers for Ag and Ag⁺ in SiO₂ are fairly different from the case of ZrO₂. As listed in Table II, the barrier is 0.61 eV for Ag atom and 0.53 eV for Ag⁺ cation. Hence, it is in principle possible for Ag⁺ to migrate to the inert electrode such that the CF starts to grow from the inert electrode. Nevertheless, even in this scenario, the morphology of the Ag CF deviates from the case of GeSe, but can be demonstrated through the model in Fig. 4(c). As experimentally reported by Yang *et al.*,²² in sputtered SiO₂ the Ag CF resembles a

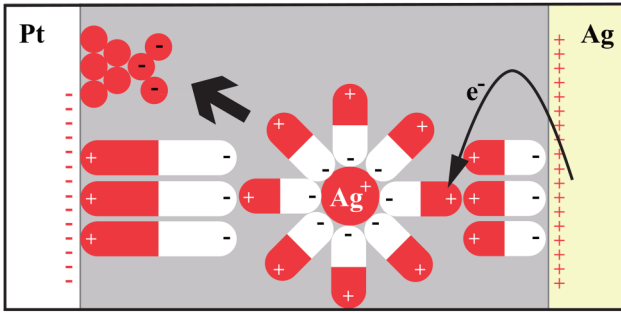


FIG. 5. The model for Ag CF growth in SiO_2 , based on a Pt/ SiO_2 /Ag cell. Around the solvated silver cation, the positive and negative bound charges are marked by red and white colors, respectively. The same color scheme is used for the general bound charges in the SiO_2 dielectric under the applied electric field. A partial Ag CF is shown on the left side of SiO_2 .

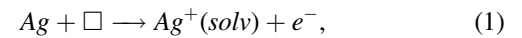
tree of Ag atoms where the root resides at the inert electrode side. In other words, although the growth direction is the same as Fig. 4(a), the shape of the CF is special because the thinnest part of the CF is no longer near the active Ag electrode in Fig. 4(c).

On the other hand, it was reported that in PECVD-obtained SiO_2 , the Ag CF has an entirely different shape,³⁷ which corresponds to the case of Fig. 4(d). The overall growth direction is from the active Ag electrode to the inert electrode. However, the CF typically consists of discontinuous Ag clusters, and mass transfer between Ag clusters gradually occurs. The overall picture is that the clusters closer to the Ag anode lose silver continuously, while the clusters closer to the inert cathode expand over time. A similar phenomenon was also discovered in evaporated SiO_2 thin films,¹³ where the lower concentration of defects implies lower mobility of Ag^+ (similar to PECVD SiO_2), compared with sputtered SiO_2 thin films. Hence, it was inferred that the mobility discrepancy causes the distinct Ag CF morphologies in PECVD/evaporated SiO_2 thin films and in sputtered SiO_2 thin films.

From the aspect of *ab initio* materials property calculation, we propose an explanation to these experimentally discovered phenomena. The key feature for silver in SiO_2 is its remarkable solvation shell as shown in Fig. 2(c). Without this shell, the positive charge carried by Ag^+ in SiO_2 is limited to a very small cation radius. Nevertheless, by carrying this shell, the area of the positive charge cloud is greatly enlarged. In sputtered SiO_2 where the migration barrier is in general lower than our calculated value 0.53 eV, Ag^+ (with +0.72 e charge according to Bader analysis) may migrate fast enough to reach the inert electrode side. However, after a partial filament has been established, the remaining solvated Ag cations tend to be attracted by the tip of the partial filament. On the one hand, the solvation shell imposes a large area of positive bound charges at its outer surface. On the other hand, the tip of the partial filament is negatively charged because it serves as the virtual cathode. Consequently, the CF ends up with a dendrite structure like Fig. 4(c).

In PECVD SiO_2 that is dense and possesses less defects, however, the migration barrier of Ag^+ is close to the 0.53 eV

value that we calculated, which is larger than that in GeSe. Hence, it is possible that the CF starts to grow from the active Ag electrode, but the morphology of the CF resembles the case of Fig. 4(d) rather than Fig. 4(b). Such a phenomenon is explained as follows. After an Ag atom is oxidized into Ag^+ that enters SiO_2 , the solvation occurs, where positive bound charges emerge in between the solvated Ag^+ and the Ag anode. Nevertheless, due to the applied electric field, inverted polarization is present within the gap between them. As a result, there are net positive bound charges present between the edge of the solvated shell and the Ag anode. These unscreened positive charges could incur strong local electric field, which leads to electron injection from the Ag anode to the solvated Ag^+ in SiO_2 (Fig. 5). The overall procedure consists of two steps:



where \square stands for an interstitial location in SiO_2 and “solv” indicates a solvated ion. The generated Ag atoms inside SiO_2 may not be exactly neutral, since the Bader charge calculation predicts that each still possesses +0.16 e , but these Ag atoms have lost their solvation sphere and their remaining charges do not strongly forbid their accumulation. After a number of Ag atoms aggregate to yield an Ag cluster near the Ag anode, the remaining charges are distributed on the surface of the cluster. It is very difficult for a massive cluster to migrate as a whole, but the individual charged silver on the surface may further migrate to the cathode side gradually. This explains the physical mechanism of mass transfer between different Ag clusters on the filament path.

D. a-Si

The a-Si supercell consists of 216 Si atoms, and an additional Ag atom has been inserted. The Ag interstitial is either neutral or +1 charged, where in the latter case we removed one electron from the supercell. The resulting Bader charges on the Ag and Ag^+ interstitials are surprisingly similar, i.e., both being +0.04 e . This implies that it is very difficult to obtain the apparently +1 charged Ag^+ inside amorphous silicon. Consequently, the directional migration of silver in a-Si is difficult, although we find that the migration barriers for Ag and Ag^+ are relatively low (both below 1 eV, shown in Table II). The silver atoms that enter a-Si thus are very probable to accumulate, not only because their migration barrier is low, but also because they carry very little charges. Hence, the generated Ag CF morphology has the pattern shown in Fig. 4(d), consisting of individual Ag clusters.

From bond length point of view, the vicinity of the silver interstitial is insensitive to the electron addition/removal. Indeed, for the apparent Ag interstitial its three shortest Ag-Si bond lengths are found to be 2.56 Å, 2.68 Å, and 2.77 Å, while for the apparent Ag^+ interstitial these lengths remain to be 2.56 Å, 2.68 Å, and 2.76 Å, resembling very much the neutral Ag interstitial case. In order to understand why Ag^+ tends to carry little charge in a-Si, we refer to

the differential charge analysis as shown in Fig. 2(d). There is no solvation shell observed, but the lost electron resides on various Si atoms with dangling bonds. In other words, there are additional electrons existing on the dangling bonds of some Si atoms, which can flow to the foreign Ag^+ , transforming it into a nearly-neutral Ag atom. Of course, structural disorder in a-Si plays a significant role in this mechanism.

E. Discussions

Our results demonstrate that while the mobility of Ag^+ is a crucial parameter that determines the morphology of Ag filaments in CBRAM, there are indeed other material properties that are significant as well. To sum up, we propose the following rules to predict the CF morphology according to *ab initio* calculation results:

- (1) Provided that Ag^+ is unstable in the dielectric, which tends to gain electron to become a neutral Ag atom, the CF grows from the active Ag electrode. A typical example is a-Si. This is because a neutral Ag atom can hardly migrate solely toward the cathode side under the applied electric field, which on the contrary only permits gradual proceeding of Ag atoms from the Ag electrode.
- (2) When Ag^+ is stable inside the dielectric and its mobility is extremely low, after entering the dielectric it tends to be reduced by leakage current. For instance, in ZrO_2 the Ag^+ migration barrier is as large as 2.48 eV such that it can be reduced to Ag atom close to the Ag anode. Consequently, the CF proceeds gradually from the Ag anode.
- (3) If Ag^+ can exist in the dielectric and its mobility is sufficiently high, then the CF grows from the inert electrode following the standard electrolyzer cell. However, there may be two types of CF morphology: (i) normal conical and (ii) dendritic. Our calculation results show that the key factor that influences the morphology is the probability of the Ag cation or its solvation shell to reach the tip of the partial filament. In case the solvation shell is large, such as Ag^+ in sputtered SiO_2 , electrochemical reduction of Ag^+ becomes much easier due to the large active surface of the solvation shell and the electrical attraction between the positively charged outer shell surface and the negatively charged filament tip. This leads to dendrite morphology. Otherwise, the Ag^+ ions typically first reach the cathode side and the filament grows by Ag atom accumulation. The morphology is therefore conical, which is common for fast cation conductors such as GeSe.

We emphasize here that the rules above can be applied in general cases, but should not be regarded as absolute. For example, even in sputtered SiO_2 , the growth direction of Ag CF may not be from the inert electrode to the active Ag electrode, given that the SiO_2 layer is very thick, as reported recently.³⁸ This is because the reduction of Ag^+ in SiO_2 is in fact permitted according to our calculations, such that Ag^+ may still be reduced after traveling a certain distance by the leakage current as electrons flow much faster than ions. Moreover, in case a large concentration of silver pre-exists in the electrolyte, or there are impurities that can serve as

nucleation centers, the possibility of Ag cluster formation will be greatly enhanced. Our calculations were mainly focused on the scenario of Ag injection into a dielectric that does not contain a large concentration of Ag initially.

V. CONCLUSIONS

For the dielectric in CBRAM, we investigated theoretically the physical mechanisms that determine the Ag conductive filament growth mode and morphology. The dielectric serves as the solid-state electrolyte, where certain properties of Ag and Ag^+ inside the electrolyte have been shown to be the key factors. The following conclusions can be drawn:

- (1) Our first finding is that the charge status of Ag interstitial in many solid-state electrolytes is fixed by the electrolyte materials. For instance, in a-Si, the Ag interstitial tends to be neutral because Ag^+ very easily captures the electrons from the dangling bonds of Si. On the other hand, in GeSe and ZrO_2 , the Ag interstitial maintains a certain amount of positive charge, the amount of which is also mainly dependent on the electrolyte material. However, in SiO_2 , there can be two distinct stable charge states for Ag, with charges of $+0.16e$ and $+0.72e$, respectively, according to the Bader analysis. Hence, in SiO_2 , the electrochemical reduction of Ag^+ may occur either at the electrode interfaces or inside the electrolyte.
- (2) Provided that Ag^+ is unstable inside the electrolyte, like the case of a-Si where Ag^+ can be reduced automatically to Ag, the CF typically consists of multiple Ag clusters inside the electrolyte, because these neutral Ag interstitials have high possibility to accumulate. Since they are almost electrically neutral, their migration is not quite directional, which promotes their horizontal movement and the accumulation.
- (3) In case Ag^+ can be stable inside the solid-state electrolyte, its mobility is the key factor to determine the direction of CF growth, which is consistent with previous reports. When the migration barrier for Ag^+ is extremely high, such as 2.48 eV for ZrO_2 , the CF can only grow from the active Ag electrode, since the ionic flux is lower than the electronic leakage current that can reduce Ag^+ near the anode surface.
- (4) In fast cation conductors such as some chalcogenides, the mobility of Ag^+ can be very high, such that the CF grows from the inert electrode. Yet, the morphology of the CF can be either conical or dendrite-like. If the cation possesses a large solvation shell that can exchange charge with the surrounding environment, and its mobility is not extremely high, dendrite CF is supposed to emerge since the solvated Ag^+ can easily be attracted to the tip of the virtue cathode made of the CF. The movement may not only be across the capacitor, but may also be in horizontal directions. Otherwise, Ag^+ tends to reach the cathode side (the cathode metal electrode or the virtue cathode) across the capacitor to render standard conical CFs.

It should be emphasized that these rules are limited to Ag CF formation, which is the simplest case because only nominally

+1 cation exists for Ag. In terms of Cu-based CBRAM, it is more complicated because a Cu cation can be either +1 or +2 charged nominally. However, the same methodology can be applied to study the Cu CF morphology in future works.

ACKNOWLEDGMENTS

This work was financially supported by the MOST of China under Grant No. 2016YFA0203800, the National Natural Science Foundation of China under Grant Nos. 11704134 and 61504045, the Fundamental Research Funds of Wuhan City under Grant No. 2017010201010106, the Fundamental Research Funds for the Central Universities of China under Grant No. HUST:2016YXMS212, and the Hubei “Chu-Tian Young Scholar” program.

- ¹S. H. Jo, T. Chang, I. Ebong, B. B. Bhadviya, P. Mazumder, and W. Lu, *Nano Lett.* **10**, 1297 (2010).
- ²X. Zhang, W. Wang, Q. Liu, X. Zhao, J. Wei, R. Cao, Z. Yao, X. Zhu, F. Zhang, H. Lv, S. Long, and M. Liu, *IEEE Electron Device Lett.* **39**, 308 (2018).
- ³L. Chua, *IEEE Trans. Circuit Theory* **18**, 507 (1971).
- ⁴D. B. Strukov, G. S. Snider, D. R. Stewart, and R. S. Williams, *Nature* **453**, 80 (2008).
- ⁵Y. Li, Y. Zhong, L. Xu, J. Zhang, X. Xu, H. Sun, and X. Miao, *Sci. Rep.* **3**, 1619 (2013).
- ⁶R. Waser, R. Dittmann, G. Staikov, and K. Szot, *Adv. Mater.* **21**, 2632 (2009).
- ⁷G.-S. Park, Y. B. Kim, S. Y. Park, X. S. Li, S. Heo, M.-J. Lee, M. Chang, J. H. Kwon, M. Kim, U.-I. Chung, R. Dittmann, R. Waser, and K. Kim, *Nat. Commun.* **4**, 2383 (2013).
- ⁸K.-H. Xue, P. Blaise, L. R. C. Fonseca, and Y. Nishi, *Phys. Rev. Lett.* **110**, 65502 (2013).
- ⁹K.-H. Xue, B. Traore, P. Blaise, L. R. C. Fonseca, E. Vianello, G. Molas, B. D. Salvo, G. Ghibaud, B. Magyari-Kope, and Y. Nishi, *IEEE Trans. Electron Devices* **61**, 1394 (2014).
- ¹⁰Y. Yang, X. Zhang, L. Qin, Q. Zeng, X. Qiu, and R. Huang, *Nat. Commun.* **8**, 15173 (2017).
- ¹¹K.-H. Xue and X.-S. Miao, *J. Appl. Phys.* **123**, 161505 (2018).
- ¹²X. Guo, C. Schindler, S. Menzel, and R. Waser, *Appl. Phys. Lett.* **91**, 133513 (2007).
- ¹³Y. Yang, P. Gao, L. Li, X. Pan, S. Tappertzhofen, S. Choi, R. Waser, I. Valov, and W. D. Lu, *Nat. Commun.* **5**, 4232 (2014).
- ¹⁴Y. Yang, Y. Takahashi, A. Tsurumaki-Fukuchi, M. Arita, M. Moors, M. Buckwell, A. Mehonic, and A. J. Kenyon, *J. Electroceram.* **39**, 73 (2017).
- ¹⁵A. Jain, S. P. Ong, G. Hautier, W. Chen, W. D. Richards, S. Dacek, S. Cholia, D. Gunter, D. Skinner, G. Ceder, and K. A. Persson, *APL Mater.* **1**, 11002 (2013).
- ¹⁶T. Fujii, M. Arita, Y. Takahashi, and I. Fujiwara, *Appl. Phys. Lett.* **98**, 212104 (2011).
- ¹⁷S.-J. Choi, G.-S. Park, K.-H. Kim, S. Cho, W.-Y. Yang, X.-S. Li, J.-H. Moon, K.-J. Lee, and K. Kim, *Adv. Mater.* **23**, 3272 (2011).
- ¹⁸Q. Liu, J. Sun, H. Lv, S. Long, K. Yin, N. Wan, Y. Li, L. Sun, and M. Liu, *Adv. Mater.* **24**, 1844 (2012).
- ¹⁹N. Banno, T. Sakamoto, N. Iguchi, H. Sunamura, K. Terabe, T. Hasegawa, and M. Aono, *IEEE Trans. Electron Devices* **55**, 3283 (2008).
- ²⁰B.-G. Chae, J.-B. Seol, J.-H. Song, K. Baek, S.-H. Oh, H. Hwang, and C.-G. Park, *Adv. Mater.* **29**, 1701752 (2017).
- ²¹R. Midya, Z. Wang, J. Zhang, S. E. Savel'ev, C. Li, M. Rao, M. H. Jang, S. Joshi, H. Jiang, P. Lin, K. Norris, N. Ge, Q. Wu, M. Barnell, Z. Li, H. L. Xin, R. S. Williams, Q. Xia, and J. J. Yang, *Adv. Mater.* **29**, 1604457 (2017).
- ²²Y. Yang, P. Gao, S. Gaba, T. Chang, X. Pan, and W. Lu, *Nat. Commun.* **3**, 732 (2012).
- ²³F. Yuan, Z. Zhang, C. Liu, F. Zhou, H. M. Yau, W. Lu, X. Qiu, H.-S. P. Wong, J. Dai, and Y. Chai, *ACS Nano* **11**, 4097 (2017).
- ²⁴G. Kresse and J. Furthmüller, *Comput. Mater. Sci.* **6**, 15 (1996).
- ²⁵G. Kresse and J. Furthmüller, *Phys. Rev. B* **54**, 11169 (1996).
- ²⁶J. P. Perdew, K. Burke, and M. Ernzerhof, *Phys. Rev. Lett.* **77**, 3865 (1996).
- ²⁷P. E. Blöchl, *Phys. Rev. B* **50**, 17953 (1994).
- ²⁸G. Kresse and D. Joubert, *Phys. Rev. B* **59**, 1758 (1999).
- ²⁹H. J. Monkhorst and J. D. Pack, *Phys. Rev. B* **13**, 5188 (1976).
- ³⁰B. Xiao, T. Gu, T. Tada, and S. Watanabe, *J. Appl. Phys.* **115**, 34503 (2014).
- ³¹N. Li and W.-Y. Ching, *XIII Int. Conf. Phys. Non-Cryst. Solids* **383**, 28 (2014).
- ³²J. S. Custer, M. O. Thompson, D. C. Jacobson, J. M. Poate, S. Roorda, W. C. Sinke, and F. Spaepen, *Appl. Phys. Lett.* **64**, 437 (1994).
- ³³M. N. Kozicki, Mira Park, and M. Mitkova, *IEEE Trans. Nanotechnol.* **4**, 331 (2005).
- ³⁴M. N. Kozicki, M. Mitkova, J. Zhu, and M. Park, *Microelectron. Eng.* **63**, 155 (2002).
- ³⁵S. Y. Shin, R. Golovchak, S. Lee, B. Cheong, H. Jain, and Y. G. Choi, *Scr. Mater.* **86**, 56 (2014).
- ³⁶S. de Souza, S. J. Visco, and L. C. De Jonghe, *J. Electrochem. Soc.* **144**, L35 (1997).
- ³⁷X. Tian, S. Yang, M. Zeng, L. Wang, J. Wei, Z. Xu, W. Wang, and X. Bai, *Adv. Mater.* **26**, 3649 (2014).
- ³⁸H. Sun, Q. Liu, C. Li, S. Long, H. Lv, C. Bi, Z. Huo, L. Li, and M. Liu, *Adv. Funct. Mater.* **24**, 5679 (2014).